

Ru-loaded pyrrolic-N-doped extensively graphitized porous carbon for high performance electrochemical hydrogen evolution

Cheol-Hwan Shin^a, Ted H. Yu^b, Ha-Young Lee^a, Byeong-June Lee^a, Soonho Kwon^b, William A. Goddard III^{b,*}, Jong-Sung Yu^{a,c,**}

^a Department of Energy Science & Engineering, Daegu Gyeongbuk Institute of Science and Technology (DGIST), Daegu 42988, Republic of Korea

^b Materials and Process Simulation Center, California Institute of Technology, Pasadena, CA 91125, United States

^c Energy Science and Engineering Research Center, DGIST, Daegu 42988, Republic of Korea



ARTICLE INFO

Keywords:

Graphitized carbon
Mg reduction
Pyrrolic-N
Hydrogen evolution
Electrochemical water splitting
Quantum mechanics calculation

ABSTRACT

Herein, we report a novel methodology for preparation of new N-doped extensively graphitized porous carbon (N-GPC) as a new catalyst support for Ru nanoparticles (NPs) with dramatically improved hydrogen evolution reaction (HER) activity. Our method is remarkably simple: pyrolyzing g-C₃N₄ in the presence of Mg metal. Here, we show that Mg plays marvelous dual roles as a reducing agent to graphitize the g-C₃N₄ precursor at low temperature and as a precursor for Mg₃N₂, which generates network-structured porous carbon as a new porogen. This offers highly robust graphitized carbon with high electrical conductivity, network-structured high porosity, and proper N content, most desired as a catalyst support. As-prepared Ru/N-GPC catalyst shows a remarkably low overpotential of 9.6 mV (vs. RHE) at 10 mA/cm², which is near ideal, providing 12 times faster hydrogen production rate than state-of-the-art Pt/C. We explain the atomistic basis for this low overpotential and superb stability via Grand canonical quantum mechanics calculations. These calculations show that pyrrolic-N in the support strengthens the coupling to the Ru NP while weakening the binding of H to Ru NP to accelerate the Tafel step.

1. Introduction

As an alternative to fossil fuels (which release to the atmosphere pollutants such as CO₂, NO_x, and SO_x upon combustion), [1–3] hydrogen energy is pollution-free and highly efficient for generating power [4–6]. Among alternatives, green energy sources such as solar, wind, and geothermal, hydrogen stands out because it is also easy to store and transport. Water splitting is considered to be the eco-friendliest technique to get hydrogen because water, the only reactant required, is plentiful when coupled to renewable sources of electricity [7–9]. Electrochemical water splitting consists of two parts;

- The hydrogen evolution reaction (HER) at the cathode side and
- The oxygen evolution reaction (OER) at the anode

The electrode is usually an active metal deposited on a supporting material in an electrochemical cell. Pt is known as the best catalyst,

leading to the Volmer-Tafel mechanism for HER with a low Tafel slope of ~ 30 mV/dec [10–12]. However, the scarcity and high expense of Pt make it impractical for extensive wide-spread applications. The material of choice as a supporting material for active catalyst nanoparticles (NPs) is porous carbon since carbon has good electronic conductivity, high surface area, high porosity, and low cost. In particular, the carbon support can be improved with heteroatom dopants (N, P or S) [13–15], increased porosity (micro, meso or macro scale) [16–18], morphologies (particle, graphene, nanotube nanofiber or 3D) [19–21], and optimized crystallinity (amorphous or graphitic) [22], all of which greatly influence the performance of the supported catalytic materials in electrochemical reactions.

Several candidates for replacing the scarce and expensive Pt have been investigated for HER. In particular, ruthenium (Ru) is considered as a promising alternative active metal. Ru has advantages of better affordability, availability, excellent activity, and durability. Several groups have reported on using Ru as a HER catalyst [23]. Ye et al.

* Corresponding author.

** Corresponding author at: Department of Energy Science & Engineering, Daegu Gyeongbuk Institute of Science and Technology (DGIST), Daegu 42988, Republic of Korea.

E-mail addresses: wag@caltech.edu (W.A. Goddard), jsyu@dgist.ac.kr (J.-S. Yu).

prepared Ru nanoclusters (NCs) anchored on B/N-doped graphene (BNG) by pyrolyzing Ru(phen)₂Cl₂ and graphene [24]. This as-prepared Ru catalyst showed an overpotential of 14 mV at a current density of 10 mA/cm² in 1.0 M KOH. Li et al. reported a mechanochemical ball-mill method to exfoliate graphite to graphene, with the exfoliated pieces of graphene loaded with Ru NPs by NaBH₄ reduction of RuCl₃ [25]. The overpotential was 33 mV in 1.0 M KOH. Lu et al. synthesized atomically dispersed Ru on the surface of carbon by a template method [26]. A low overpotential of 12 mV was reported at 10 mA/cm² in 1.0 M KOH owing to the formation of RuC_xN_y moieties as single atom active centers. However, further improvements are required for commercialization of the Ru-based catalysts (simplifying the complex preparation method and improving long-term stability). Furthermore, the role of **supporting material** has not yet been sufficiently investigated. In particular, the beneficial effects of improved graphiticity for high conductivity and dopant-induced optimization of the surface charge distribution have not yet been thoroughly explored for carbon-supported metal HER catalysts.

Three key features are most desired in a carbon support for electrolysis:

- Graphiticity for high electronic conductivity and stability,
- Porosity for high surface area and mass transfer, and
- Heteroatom doping for activity and synergistic effects.

The treatment temperature plays a key role in controlling all three features [27]. Usually, graphitic carbons are prepared by high temperature pyrolysis of organic precursors to attain graphiticity [28–30], but most carbon materials prepared lower than 1000 °C display still low levels of graphiticity; high graphiticity requires pyrolysis at temperatures > 2000 °C [31]. However, because of thermally-induced tight cross-linking, carbons prepared at such high temperatures usually show low porosity, which hinders an effective mass transport [32,33]. Synthetic approaches that create sufficient porous structures are usually carried out through template methods employing sacrificial hard (silica or other inorganic solids) or soft (polymers) templates. Removal of template after carbonization gives a variety of mesopores or/and macroporous pores or channels in the carbon framework for interfaces between catalysts and electrolytes and mass transfer [34,35]. Analogously, nitrogen doping into the carbon provides synergistic effects for electrocatalytic reactions, improving both durability and activity of the supported catalyst metal [36,37]. Increasing temperature increases graphiticity, conductivity and structural stability, but decreases both N content and porosity, making optimum control over these key factors in carbon synthesis seemingly not possible.

To address these issues, we report here the first N-doped porous carbon with high graphiticity, synthesized via a simple pyrolysis using graphitic carbon nitride (g-C₃N₄) as a precursor for carbon and nitrogen in the presence of Mg metal. In this work, Mg with high reducing capability effectively removes much of the N from the precursor during carbonization to generate Mg₃N₂, while the N-detached carbon atoms

quickly make bonds to generate a highly graphitized carbon framework (See Fig. 1) [38,39]. Interestingly, here the Mg plays a marvelous dual role not only as a reducing agent for graphitizing the carbon precursor at low temperature but also as a precursor for a new Mg₃N₂ product. This generated Mg₃N₂ serves as a new pore-generating agent in this work, like MgO often used as a pore generating template in earlier carbon synthesis [34,35]. Indeed, post-carbonization HCl etching dissolves out excess Mg and Mg₃N₂, leaving behind mainly meso- and macropores in the resulting graphitized network-structured carbon framework. Sufficient N atoms survive the Mg-induced carbonization to generate N-doped highly graphitized carbon (N-GPC) with a highly porous network structure. Ru was then loaded on the as-prepared N-GPC. The Ru-carbon composite was then treated with NH₃ gas to reduce the ionic Ru to metallic Ru NPs. This as-prepared Ru-loaded N-GPC (Ru/N-GPC) was investigated for HER performance under alkaline condition. In addition, we used quantum-mechanics (QM) based calculations and various physicochemical probes to establish the mechanism underlying the dramatically improved interactions between N-species in N-GPC and the Ru NPs.

2. Results and discussion

2.1. Synthesis and features of N-GPC

The synthesis procedure is illustrated in Fig. 1. (the details are found in [Supporting Information, SI](#)). Fig. S1a and b in SI exhibit transmission electron microscopy (TEM) images of bare g-C₃N₄ showing thin-layered structures with an amorphous surface. However, nothing remains probably because of thermal decomposition of the g-C₃N₄ during the high temperature pyrolysis at 950 °C for 5 h without Mg metal. In contrast, pyrolysis of g-C₃N₄ heated at identical conditions with Mg metal leads to black powder. After magnesiothermic (Mg-annealing) carbonization and acid etching, we observe N-GPC with highly graphitic crystalline structures, 7–15 stacked graphene layers along with thin 1–2 graphene layers and medium 3–7 graphene layer stacks, all with a lattice distance of 0.34 nm consistent with the graphite layer spacing (see Fig. S1d and e) [40].

To better understand the role of Mg during synthesis, the sample was analyzed before and after acid etching. Fig. S2 displays high angle annular dark field-scanning transmission electron microscopy (HAADF-STEM) images and energy dispersive spectroscopy (EDS) mapping images of g-C₃N₄ and N-GPC before and after etching. Mg and N can be seen densely covering the whole surface of N-GPC before etching, whereas they dramatically decrease with almost no Mg seen after etching ([Table S1](#)). X-ray diffraction (XRD) in Fig. S3 shows the products at each synthesis step. The g-C₃N₄ leads to peaks at 13.1° from the (100) planes for ordered C-N ring configurations and at 27.6° from the (002) planes for the graphite-like structure [41]. New strong signals corresponding to Mg₃N₂ (JCPDS card 35–0778) are observed after Mg treatment and before etching, showing that Mg takes N from g-C₃N₄.

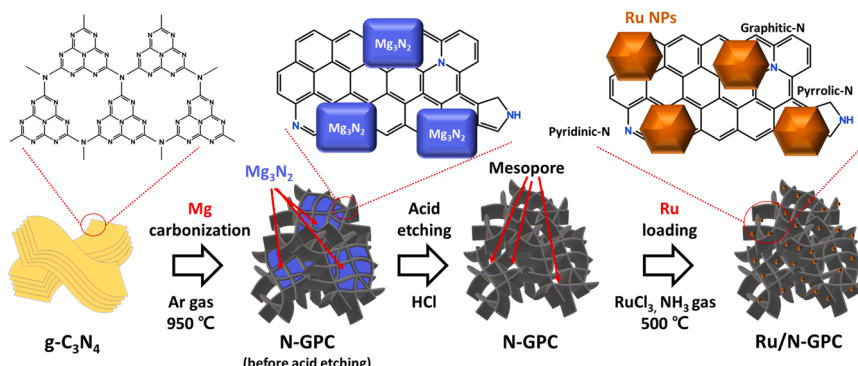


Fig. 1. Schematic synthesis procedure for Ru/N-GPC.

during Mg pyrolysis to form Mg_3N_2 . Interestingly, the newly generated Mg_3N_2 plays a key role as a new pore-generating agent for the resulting porous carbon. In earlier work, MgO directly added or derived from Mg acetate was employed as a pore-generating agent to increase mesopores in the resulting carbon framework [33–35]. In our new work, we introduce a novel synthesis approach employing Mg, which has a remarkable dual role not only as a reducing agent for enabling graphitized carbon framework at low temperature (even at 650 °C) but also as a precursor for our new Mg_3N_2 template. Thus, due to the in-situ generation of Mg_3N_2 as a porogen during the reaction, we do not need a separate pore-generating agent or precursor to attain high porosity. After acid etching, all strong Mg_3N_2 signals disappear, while an intense (002) signal at 26.5°, typical of graphite, develops predominantly along with some amorphous phase at 18–23° in as-prepared N-GPC. At the same time, the acid etching leaves behind mainly meso- and macropores in the resulting graphitized carbon framework as shown in Fig. S4.

The physicochemical properties of carbon materials depend highly on the carbonization temperature and time [33,37]. Thus, the magnesiothermic pyrolysis of $g\text{-}C_3N_4$ precursor was done at both 650 and 1150 °C to examine temperature effects in addition to pyrolysis at 950 °C. In general, a higher pyrolysis temperature increases the graphitization of carbon. The samples prepared at 650 and 1150 °C are denoted as N-GPC-65 and N-GPC-115, respectively. The N-GPC and N-GPC-115 exhibit well-developed open network structure of mesopores (2–50 nm) and macropores (>50 nm) due to the templating role of the Mg_3N_2 products compared to N-GPC-65 prepared at lower temperature.

XRD patterns indicate that higher magnesiothermic pyrolysis temperature makes carbon more graphitic as shown in Fig. 2a. Interestingly, both N-GPC and N-GPC-115 display development of a broad signal near at 18–23°, corresponding to an amorphous carbon phase, along with predominant development of the graphitic (200) signal at 26.5°, while N-GPC-65 shows a very weak amorphous phase at the same range. The

broad peak seems to be due to formation of randomly distributed thin carbon layer structures with increasing carbonization temperature. The generation of such amorphous phase is related to the structuring process of open network of meso- and macropores during graphitization with help of Mg at relatively high temperatures of 950 °C and higher (Fig. S1c-d and Fig. S4). However, this structuring process is not yet to be started in N-GPC-65 prepared at lower temperature of 650 °C which rather resembles the pristine $g\text{-}C_3N_4$ with thick and bulk-like structure (Fig. S4 and Fig. S5a-b).

Raman spectrometer was employed for further analyzing graphitic structures in carbon samples. Absorption peaks at ~1360, 1560 and 2700 cm⁻¹ indicate disordered C-sp³ (D peak), graphitic C-sp² (G peak), and high ordered graphene (2D peak), respectively [42,43]. All the N-GPC samples show high G peak and 2D peak, revealing that the N-GPC samples has a high graphitic structure. By calculating ratios of I_D/I_G and I_{2D}/I_G , the graphiticity degree could be evaluated. N-GPC displays a marked highly intense graphitic C-sp² G peak relative to disordered C-sp³ D peak. Furthermore, an unusual 2D peak, observed only in highly graphitized carbon, develops strongly at ~2700 cm⁻¹. N-GPC-115 shows a much lower I_D/I_G ratio of 0.20 and a higher I_{2D}/I_G ratio of 1.85 than N-GPC-65 ($I_D/I_G=0.57$ and $I_{2D}/I_G=0.92$) and N-GPC ($I_D/I_G=0.32$ and $I_{2D}/I_G=1.80$) as shown in Raman spectra (Fig. 2b). The low I_D/I_G ratio and formation of the 2D signal in the Raman spectrum is a striking feature for the relatively low carbonization temperature of 950 °C, strongly supporting the high graphiticity of N-GPC. With the higher magnesiothermic pyrolysis temperature, the lower Brunauer–Emmet–Teller (BET) surface area (Fig. S6); 360.6 m²/g for N-GPC-65, 234.4 m²/g for N-GPC and 182.3 m²/g for N-GPC-115. The N-GPC-65 possesses more of smaller mesopores and micropores which are explicitly not exposed on the surface, which makes it look less porous compared to the N-GPC.

Electrical conductivity was measured using home-made four probe

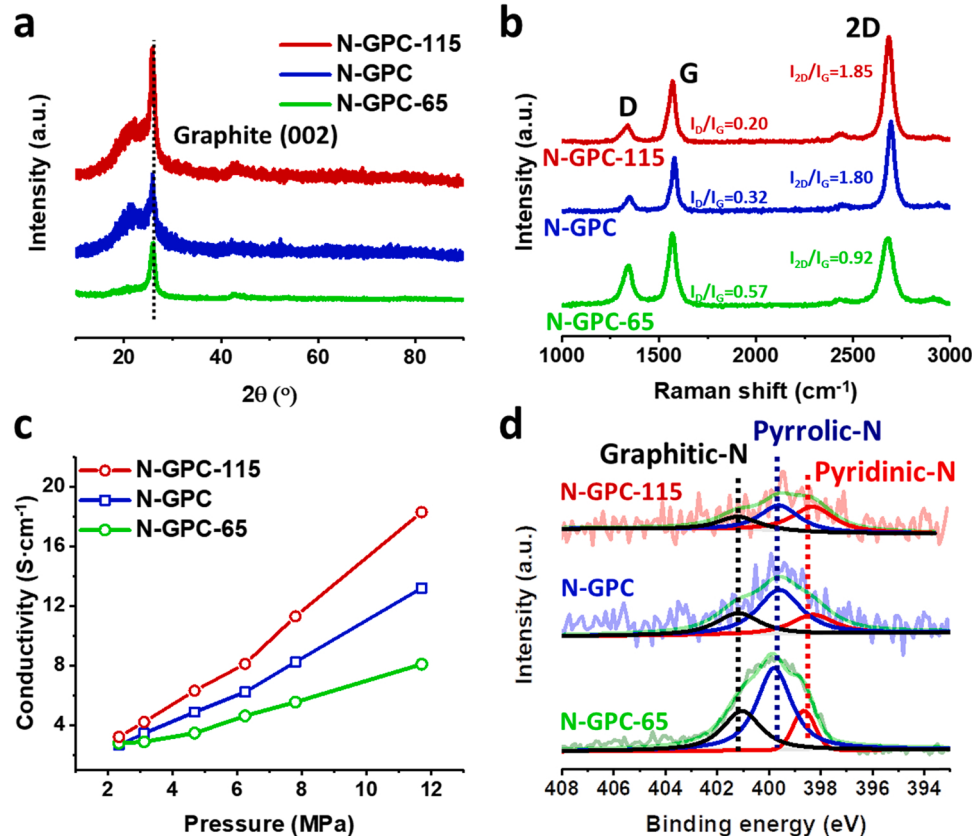


Fig. 2. N-GPC samples prepared at different temperatures. (a) XRD patterns, (b) Raman spectra, (c) electrical conductivity profiles, and (d) high-resolution N 1 s XPS profiles for the different samples.

configuration system. The detailed analysis method is explained in Experimental section of Supporting Information. The electrical conductivity increases with increasing temperature because of a higher degree of graphitization (Fig. 2c). In contrast, the parent g-C₃N₄ shows almost no conductivity (Fig. S14c). Due to different treatment conditions, the carbons produced from g-C₃N₄ in earlier works were not fully graphitized, with much less pronounced graphitic (002) XRD signals and higher I_D/I_G values compared to the present work [29,30]. This present work is the first to demonstrate development of N-doped highly graphitized carbon with a highly porous network structure from g-C₃N₄.

To discuss on chemical structure of N-GPC samples, X-ray photoelectron spectroscopy (XPS) analyses were conducted, and all the obtained signals were corrected by C 1 s at 284.8 eV as a calibration point. Fig. 2d exhibits high-resolution N 1 s XPS spectra of different N-GPC samples which can be deconvoluted into pyridinic-N (~398.3 eV), pyrrolic-N (~399.4 eV), and graphitic-N (~401.3 eV) [44,45]. This predominant development of pyrrolic-N is quite interesting because pyrrolic-N is usually weakly observed at carbonization temperature near 900 °C and decreases quickly with increasing temperature. Indeed, the pyrrolic-N content is found to be 68% for N-GPC-65, 55% for N-GPC, and still dominant with 36% N-GPC-115 (although decreasing with increasing temperature). Since graphitic-N and pyridinic-N have been known to be more favorable than pyrrolic-N at temperature higher than 900 °C, the N-GPC samples are quite unique in retaining a high content of pyrrolic-N [46]. The total amount of N dopants decreases with increasing carbonization temperature (Table S3). This represents the first report of the efficient synthesis of the highly graphitized carbon with proper N doping at relatively low temperature below 1000 °C.

2.2. Physicochemical features and HER performance of Ru-loaded N-GPC

Ru NPs were deposited on N-GPC through NH₃ reduction at 500 °C of

Ru³⁺ ions loaded by a simple impregnation method with RuCl₃. Fig. 3 shows HAADF-STEM images and EDS mapping images of Ru/N-GPC. We find that Ru/N-GPC possesses a porous network structure including large mesopores with diameters of 20–50 nm and macropores in the range of 50–200 nm developed homogeneously on the surface. Such 3D net-like morphology is advantageous for mass transfer during electrochemical reactions [47,48]. The magnified image (Fig. 3b) shows that Ru NPs with a size of 2–4 nm are well dispersed over the N-GPC framework with a lattice parameter of 0.205 nm associated with the hexagonal close packed (HCP) Ru (101) phase [49]. This is consistent with the TEM images (Fig. S7). EDS mapping images corresponding to the STEM image in Fig. 3c indicate that the Ru/N-GPC consists of well-dispersed N dopants in addition to C and Ru. The element ratio was found to be 9.3 wt% for Ru, 89.3 wt% for C, and 1.4 wt% for N from EDS mapping.

Fig. 4a shows the XRD patterns of various samples prepared in this work. A broad peak at 40–44° is developed for Ru-loaded N-GPC (Ru/N-GPC), indicating the deposition of small Ru NPs with HCP crystal structure on the carbon [49]. The strong and sharp graphitic carbon peak at 26.5° is still maintained after loading Ru NPs, while the broad amorphous carbon signal near at 18–23° decreases probably because of preferential etching of the amorphous carbon by NH₃ gas used for Ru loading at 500 °C. The carbon structure was further analyzed by Raman spectroscopy in Fig. 4b. The g-C₃N₄ does not show any meaningful Raman signal, indicating that the g-C₃N₄ does not feature the general carbon character. In contrast, the N-GPC displays a low I_D/I_G ratio of 0.32 along with a strong 2D peak. After Ru loading, the I_D/I_G ratio increases to 0.86 along with a decrease of the G peak. The 2D signal also decreases with an I_{2D}/I_G ratio of 0.68, indicating some decrease of graphiticity. This decrease is attributed to the heat treatment under NH₃ gas during Ru loading, which can increase defects/disorder on the graphitic layer. However, the G and 2D peaks are still strong in

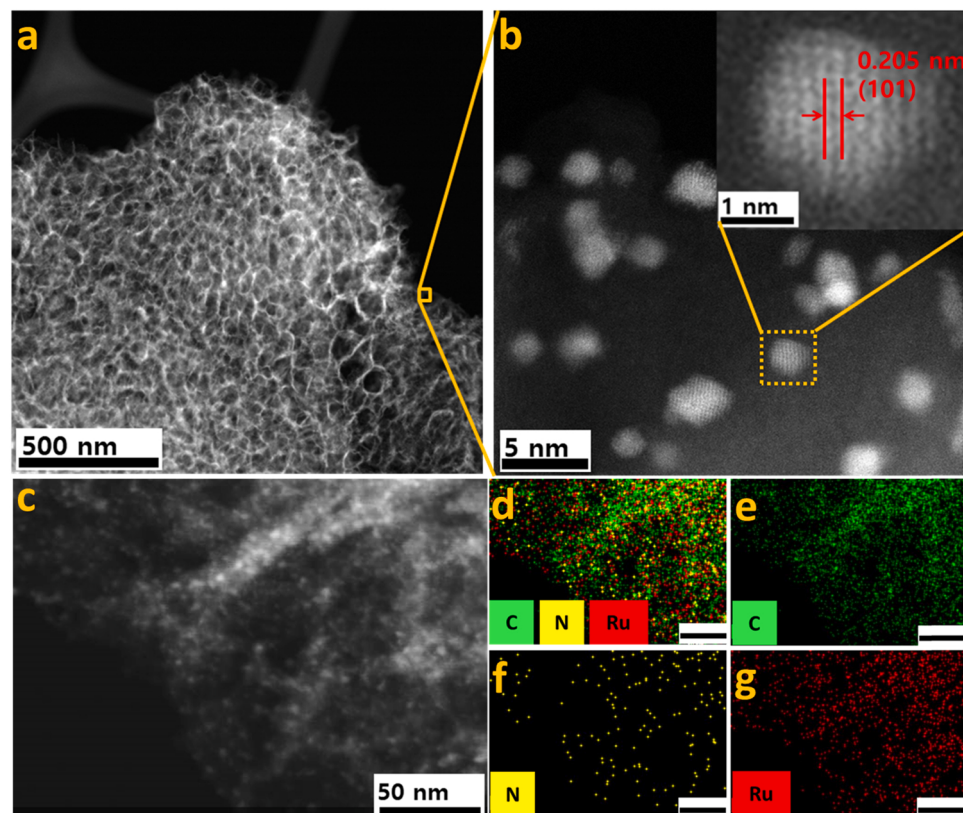


Fig. 3. Morphologies and element composition of Ru/N-GPC. (a-b) High-resolution HAADF-STEM images and (c) STEM image of Ru/N-GPC. (d-g) Corresponding elemental mapping images of Ru/N-GPC (scale bar: 50 nm in Fig. 3d-g).

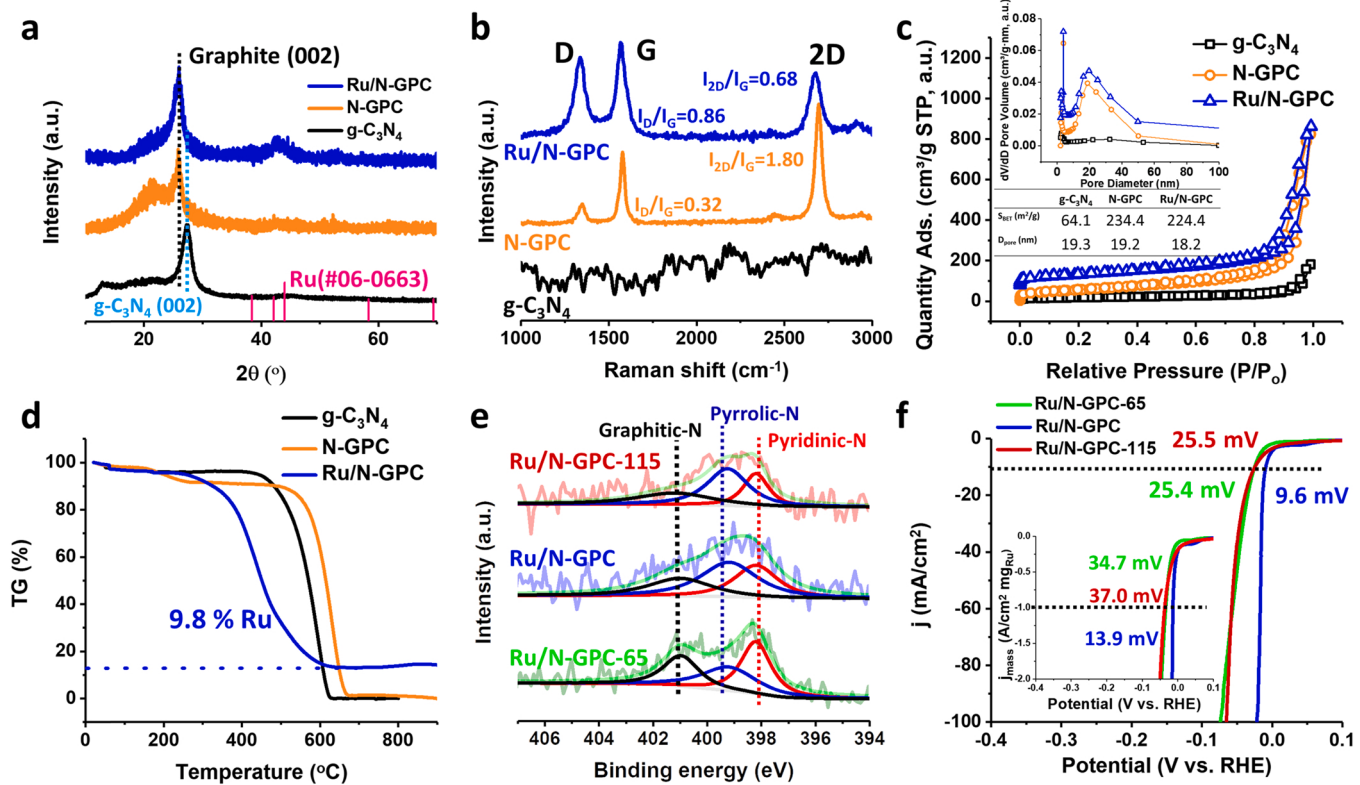


Fig. 4. Chemical features and electrochemical performance of Ru/N-GPC. (a) XRD patterns, (b) Raman spectra, (c) N₂ adsorption/desorption isotherms, (d) TGA profiles under air atmosphere for various samples. Inserts in Fig. 4c show pore size distribution and a table for surface area and average pore diameter. (e) High-resolution XPS spectra of N 1 s, and (f) HER linear sweep voltammetry (LSV) curves for Ru-loaded N-GPC samples. All electrochemical measurements were performed in 1.0 M KOH. The insert in Fig. 4f is the mass activity.

Ru/N-GPC, indicating that the Ru/N-GPC retains highly crystalline graphene layers [42,43].

N₂ adsorption/desorption isotherms (Fig. 4c) indicate the N-GPC shows a higher BET surface area of 234.4 m²/g compared to 64.1 m²/g for bare g-C₃N₄ (probably because of pore generation during magnesiothermic carbonization). The isotherm behavior of N-GPC from 0.80 to 0.99 P/P₀ is attributed to mesopores and macropores developed in the carbon framework [50]. Interestingly, the Ru/N-GPC made little change on the isotherm pattern, showing almost identical isotherm behavior to N-GPC with a similar BET surface area of 224.4 m²/g. The insert in Fig. 4c displays an average pore size distribution of ~19 nm for all samples. Ru metal does not dissolve in any medium such as strong acidic or basic solutions. Hence, to determine the Ru loading amount, thermogravimetric analysis (TGA) was carried out under air atmosphere (Fig. 4d). The Ru loading of Ru/N-GPC was determined to be 9.8 wt%.

Fig. S8a shows the survey scan XPS spectra for the C, N, and O in 1 s orbitals. After Ru loading, Ru signals appear at ~281 eV (3d orbitals) and ~460 eV and ~490 eV (3p orbitals). High-resolution XPS spectra of C 1 s and Ru 3d (Fig. S8b) clearly reveal the presence of metallic Ru at 280.9 eV for Ru/N-GPC [25]. The high-resolution XPS spectra of N 1 s can be deconvoluted into several N species (Fig. S8c). After Ru loading, the Ru/N-GPC shows slight shift to lower binding energy, indicating a strong interaction of N-species in N-GPC with Ru. Table S2 summarizes deconvolution analysis of N 1 s spectra in N-GPC and Ru/N-GPC.

Ru NPs were also loaded on the carbon samples prepared at 650 and 1150 °C by the identical method, with the samples denoted as Ru/N-GPC-65 and Ru/N-GPC-115, respectively. The Ru/N-GPC-65 and Ru/N-GPC-115 (Fig. S9) show Ru NPs with 2–4 nm in size, similar to Ru/N-GPC (Fig. S7). This matches well with XRD patterns showing a weak broad peak at 40–42 (Fig. S10a). Raman spectra (Fig. S10b) reveals that graphiticity decreases a bit for all the samples after Ru loading due to the etching effect of the NH₃ gas used for Ru deposition. The surface area

(Fig. S10c) and electrical conductivity (Fig. S10d) are found to be similar before and after the Ru loading (Table S4). The Ru-loaded N-GPC samples have Ru loading of 8–10 wt% (Fig. S10e).

High-resolution XPS spectra of N 1 s (Fig. 4e) show somewhat complex changes after Ru loading. The pyridinic-N becomes a major species for the Ru/N-GPC-65, while the pyrrolic-N low for the Ru/N-GPC-65 gradually increases for the Ru/N-GPC and Ru/N-GPC-115 compared to the pyridinic and graphitic N species. The deconvoluted N 1 s spectra before and after Ru loading over N-GPC synthesized at different temperatures are summarized in Table S2. Interestingly, the relative pyrrolic-N content decreases, while the pyridinic and graphitic-N contents increase before Ru loading for increasing carbonization temperature, whereas the situations get reversed after Ru loading, i.e., the pyrrolic-N content increases, while the pyridinic and graphitic-N contents decrease for the higher temperature. This is quite interesting and seems probably due to some interchange between different N species during NH₃ gas treatment for the Ru loading. XPS analyses before and after Ru loading over N-GPC samples are summarized in Table S3. All the Ru-loaded samples possess metallic Ru (Fig. S10f).

HER performance was evaluated by linear sweep voltammetry (LSV) as illustrated in Fig. 4f. In this study, the LSV curves were obtained after stabilization process by CV cycling in the potential range from 0.1 to -0.4 V for ~20 times. Ru/N-GPC has an overpotential of only 9.6 mV, much lower than Ru/N-GPC-65 (25.4 mV) and Ru/N-GPC-115 (25.5 mV) at a current density of 10 mA/cm². The Ru/N-GPC also shows a higher mass activity of 13.9 mV at 1 A/cm² mg_{Ru} than Ru/N-GPC-65 (34.7 mV) and Ru/N-GPC-115 (37.0 mV). The superior HER performance of Ru/N-GPC prepared at 950 °C may be ascribed to the well-balanced structural properties of the supporting carbon including porous structure for mass diffusion, high electronic conductivity, and proper N content in the highly graphitized carbon framework. In fact, the N-GPC possesses almost all the top-quality properties necessary as a

superb supporting carbon for HER through a simple Mg treatment. With the N-GPC support, first, the loading amount of Ru was optimized for HER, with the sample denoted as Ru(x)/N-GPC, where x is the amount of Ru used; 0.125 ml 0.25 ml, and 0.5 ml RuCl₃ solutions (20 mg Ru³⁺/ml) were used for Ru(0.5)/N-GPC, Ru/N-GPC, and Ru(2)/N-GPC, respectively. The Ru/N-GPC possesses optimum properties for HER compared to the other Ru-loaded N-GPC samples with different Ru amounts (Figs. S11 and S12). Linear sweep voltammetry (LSV) curves indicate that Ru/N-GPC shows a higher activity and mass activity than Ru(0.5)/N-GPC and Ru(2)/N-GPC (Fig. S12c-d).

2.3. Comparisons with other carbon supports

Other commonly used carbon supports such as.

- commercial Vulcan carbon XC-72 (VC)
- Ketjen balck EC600JD (KB), and
- as-prepared N-doped reduced graphene oxide (N-rGO)

were also tested for comparison [51]. The physicochemical features of these carbon supports are described in Figs. S13 and S14.

Ru NPs were also loaded over VC, KB, and N-rGO using the method identical to the synthesis of Ru/N-GPC. Interestingly, Ru NPs loaded over VC and KB are relatively larger with approximately 10–20 nm in size (Fig. S15a and b), whereas Ru/N-rGO displays much smaller Ru NPs with 2–4 nm, which is similar to that of Ru/N-GPC (Fig. S7 and S15c). This may indicate that Ru particle size is related to N dopants in the carbon support framework. The N sites may help Ru become distributed homogeneously with smaller particle size over the support because of interaction between the electronegative N and electropositive Ru³⁺ ion. XRD patterns, Raman spectra, electrical conductivity profiles, and N2 adsorption/desorption profiles of different carbon supports with Ru loading are shown in Fig. S16a-e. The surface properties of before and after Ru loading are summarized in Table S4. The Ru loading amount of each sample was confirmed by TGA as illustrated in Fig. S17a.

Different carbon supports loaded with Ru NPs were also analyzed by XPS (Fig. S17). Interestingly, high-resolution N 1 s XPS spectra (Fig. S17c) show that both Ru/N-rGO and Ru/N-GPC have similar N bonding structure, but with a different ratio between different N species (Table S5). In addition, the Ru⁰ peaks of Ru/N-GPC and Ru/N-rGO are positively shifted by ~ 0.6 eV compared to those of Ru/VC and Ru/KB with no N doping in Ru 3d XPS spectra as shown in Fig. S17d. In fact, the XPS profile in Ru 3d overlaps with that of C 1 s, making it difficult to determine Ru oxidation states from the Ru 3d spectrum. To resolve this curiosity, we further analyzed Ru 3p XPS spectra. Fig. S17e displays the Ru 3p XPS spectra, and all the prepared samples show two peaks at ~462.5 eV for metallic Ru as a major species and at ~464.7 eV for RuO₂ as a minor. Interestingly, the trend of positive shifting by around ~0.7 eV observed for the Ru/N-rGO and Ru/N-GPC in Ru 3p XPS spectra is similar to that shown in Ru 3d spectra. This is a clear evidence that N dopants in carbon framework have an influence on the electron energy distribution of Ru. In d-band theory, the positive shifting in XPS means the downshifting of a d-band center from the Fermi level, which allows the anti-bonding orbital to have more electrons compared with unshifted one. The more electrons in the anti-bonding orbital mitigate the strong hydrogen binding energy of Ru catalysts, resulting in improvement of HER activity [52]. Fig. S17f illustrates the O 1 s XPS spectra of Ru-loaded samples with different carbon supports. The XPS spectra were deconvoluted to three peaks at 531.4, 532.6, and 533.8 eV for Ru-O, C-O, and H-O-H, respectively [53]. The formation of Ru-O may be caused by the absorbed oxygen or moisture from air on the Ru NPs. The Ru/N-rGO and Ru/N-GPC exhibits a higher peak intensity of Ru-O compared with the Ru/VC and Ru/KB. This is ascribed to the smaller size of Ru NPs on the Ru/N-rGO and Ru/N-GPC, which results in the higher surface area of the Ru NPs, than that of the Ru/VC and Ru/KB. This is well matched with TEM images as shown in Fig. S11 and S15.

Fig. 5a exhibits LSV curves for HER, where the N-GPC sample shows almost no activity without Ru loading, indicating that N-doped carbon is not active for HER. On the other hand, Ru-loaded N-GPC (Ru/N-GPC) performs extraordinarily with an overpotential (at a current density of 10 mA/cm²) of only 9.6 mV, much lower than that (39 mV) of state-of-the-art commercial 20% Pt/C (Tanaka Holdings Co., Ltd.), clearly indicating that Ru is active for HER. Based on the difference in loading amount and atomic mass of active metal elements for Ru/N-GPC and commercial 20% Pt/C, we calculated the turnover frequency (TOF) and mass activity. Fig. 5b shows the TOF and mass activity profiles corresponding to the LSV curves in Fig. 5a. Ru/N-GPC shows the TOF and mass activity with 1.31×10^{-3} s⁻¹ at -0.025 V_{RHE} and 13.9 mV at 1 A/cm² mg_{metal} which are much better than those (0.11×10^{-3} s⁻¹ at -0.025 V_{RHE} and 73.1 mV) of Pt/C. Generally, the TOF value indicates the reaction speed in the catalyst system, suggesting that the hydrogen production rate of the Ru/N-GPC is about 12 times faster than that of state-of-the-art Pt/C [25].

HER activity was examined for the different supports for Ru catalyst recorded using catalyst-coated glassy carbon electrode in Fig. 5c. Compared to commercial 20% Pt/C,

- Ru/KB and Ru/VC display lower activity, but
- Ru/N-rGO and Ru/N-GPC with N dopants in the carbon framework reveal higher activity.

Ru/N-GPC shows the best HER activity among all carbon-supported Ru catalysts. It also displays the lowest overpotential among other samples in terms of the mass activity (Fig. S18). Ru/N-rGO also shows very good HER activity next to Ru/N-GPC. These results indicate that N dopants in carbon play important roles in promoting HER activity of Ru NPs. The poor activity for Ru loaded onto undoped carbon support such as KB and VC may be partially attributed to the large particles. The superb HER performance of Ru/N-GPC is attributed both to the well-dispersed small Ru NPs and to the highly beneficial structural effects such as high graphiticity, N dopants, and well-developed open porous structure of N-GPC support. Furthermore, Ru/N-GPC displays the lowest Tafel slope of 25.2 mV/dec among all samples prepared as shown in Fig. 5d. This lower value of 25.2 mV/dec indicates that the HER mechanism follows Volmer-Tafel steps [52]. Electrochemical impedance spectra (EIS) disclose that the Ru/N-GPC has lower charge transfer resistance among other samples (Fig. S19). Electrochemical double layer capacitance (EDLC, C_{dL}) profiles and CV cycles between 0.0 and 1.2 V reveal that the Ru/N-GPC has more active sites available to accept hydrogen ions and then to reduce them to hydrogen gas (Figs. S20 and S21) [54,55]. Table S6 summarizes HER performance of different samples tested in this study.

A stability test was carried out by chronopotentiometry using catalyst-coated carbon paper as illustrated in Fig. 5e. The initial overpotentials of Ru/N-GPC and 20% Pt/C were 12 and 34 mV, respectively. After 200 h, the overpotentials increase slightly for both Ru/N-GPC (19 mV) and 20% Pt/C (45 mV). The step stability tests were conducted through chronopotentiometry under different current densities of 10, 50, and 100 mA/cm², each for 25 h, and then returned to 10 mA/cm². The Ru/N-GPC maintains almost identical overpotential at each step, showing excellent stability even at high current density without any degradation in Ru NPs (Fig. 5f). Fig. S22a and b exhibit that the particle size and distribution of Ru NPs are well maintained without any significant change after the chronopotentiometry test at 10 mA/cm² for 200 h compared to fresh Ru/N-GPC sample.

An accelerated durability test (ADT) was also conducted by CV over a range from 0.1 to -0.4 V_{RHE} for 10,000 cycles. Fig. S23 exhibits the LSV curves before and after 10k CV cycles of each sample. Notably, the Ru/N-GPC shows superb durability of $\Delta E = \sim 0$ mV compared to that of 20% Pt/C ($\Delta E = 7$ mV) after 10k cycles in agreement with Fig. 5e and f, demonstrating the superb durability of the Ru/N-GPC. Fig. 5g and Table S7 summarize HER performances for comparison with other

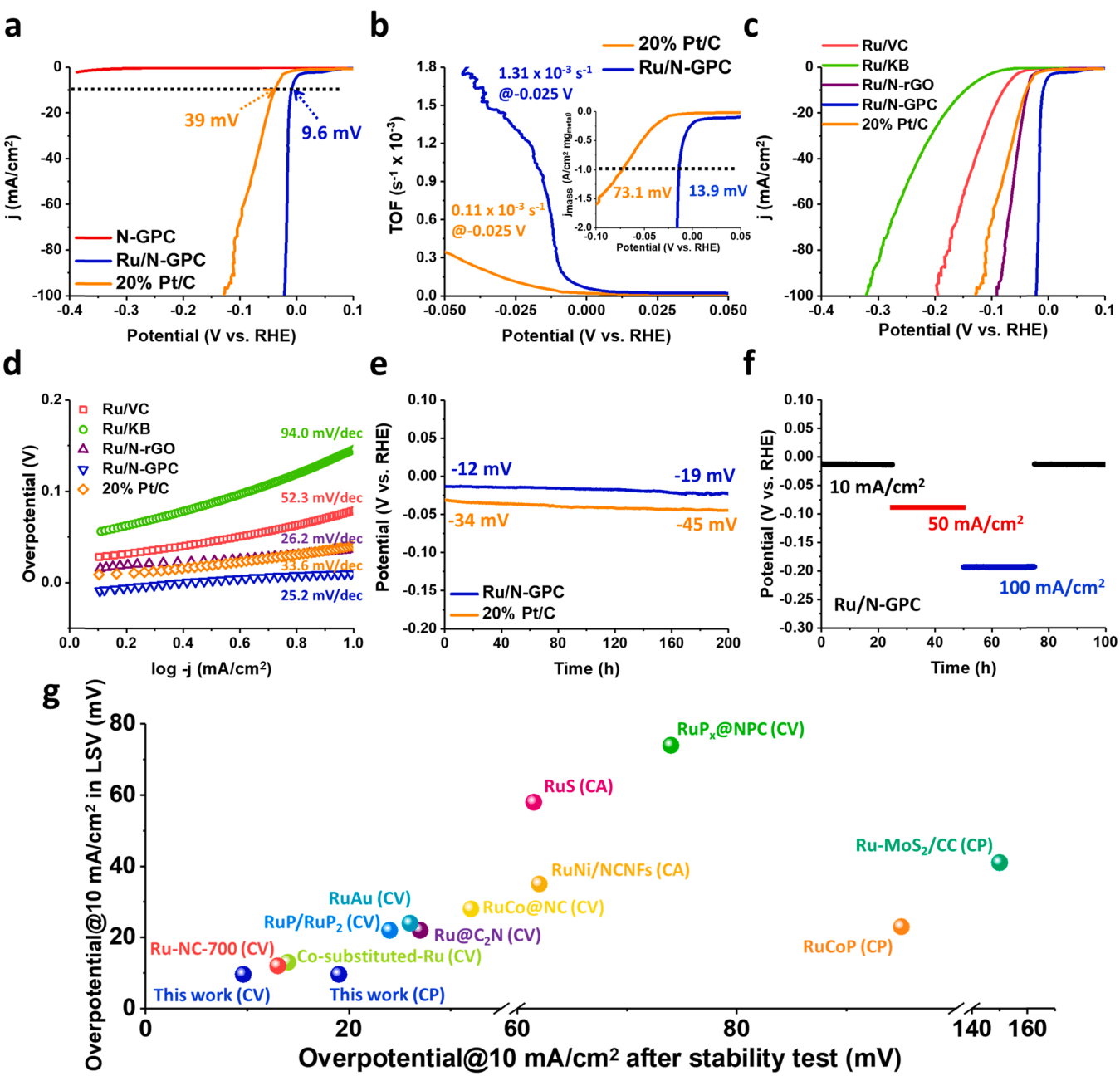


Fig. 5. HER performance of Ru/N-GPC. (a) HER LSV curves, (b) TOF profiles (insert is the mass activity), (c) HER LSV curves, (d) Tafel plots, (e) chronopotentiometry profiles at a current density of 10 mA/cm^2 , (f) step stability tests under current densities of 10, 50, and 100 mA/cm^2 for different samples prepared in this work. (g) Overpotentials at 10 mA/cm^2 in LSV and after stability test (CV: cyclic voltammetry, CP: chronopotentiometry, and CA: chronoamperometry) of Ru/N-GPC compared with other samples in the literature. All electrochemical measurements were performed in 1.0 M KOH. In Fig. 5a and c, LSV curves were recorded using catalyst-coated glassy carbon electrode (electrode area: 0.196 cm^2 and loading amount: 0.21 mg/cm^2), while in Fig. 5e and f, chronopotentiometry and step stability tests were recorded using catalyst-coated carbon paper (electrode area: 1 cm^2 and loading amount: 0.21 mg/cm^2).

studies in literature [26,56–66]. Clearly, Ru/N-GPC demonstrates the most active and durable HER performance among the works reported in literature to the best of our knowledge. Ru single atom catalysts as well as Ru NPs supported on the conductive carbon were also reported to be very active for HER in alkaline condition [26]. Based on the experimental conditions and analyses, we believe that the generation of Ru single atom catalysts on the N-GPC support is very unlikely during the current synthesis procedure. However, there may be still some possibility for the formation of single atoms on the carbon during Ru loading process. Even with such case, the number of single atom catalysts would be very little, and thus their contribution to the HER activity would be very minor if any.

2.4. Quantum mechanics-based analysis of the HER mechanisms in Ru/N-GPC

In order to understand the atomistic origins of the high activity and stability of the Ru/N-GPC catalysts in HER, we carried out a series of quantum mechanics (QM) calculations using density functional theory (DFT) with the Perdew-Burke-Ernzerhof functional with D3 London dispersion interactions (PBE-D3) [67,68].

We started with a periodic 4×4 graphene surface model with 50 C atoms and considered 4 cases:

- graphene, and nitrogen dopants to create defects

- b. pyrrolic-N, Fig. 6ai
- c. graphitic-N, Fig. 6aii
- d. pyridinic-N, Fig. 6aiii

The Ru (HCP, 0001) phase has been known to possess the best water dissociation ability during HER in alkaline condition [69]. On top of the graphene surfaces, we placed three layers of Ru (HCP, 0001) using the $\sqrt{13}x\sqrt{13}$ surface (Fig. 6a) in order to have a good lattice match (9.84 vs. 9.76 Å). This leads to 39 Ru atoms on top of 32 atoms of undoped or N-doped graphene. We optimized the number of H atoms binding to the Ru(0001) surface (1–13) and predicted the barrier to remove H₂ (Tafel reaction) at different concentrations. To include the effect of water solvent and applied electrode potential, we used the grand-canonical quantum mechanics (GC-QM) method (also referred to as Grand Canonical Potential - Kinetics (GCP-K)) [70,71]. GC-QM predicts the free energies as a function of applied potential, U, (Fig. S24).

We first calculated the barrier to remove H₂ (Tafel step) from a fully saturated Ru-N-graphene surface as shown in Fig. 6b. The experimental Tafel slope < 30 mV/dec indicates that the mechanism is Volmer-Tafel [72]. The potential dependence of the HER reaction may arise from the change in hydrogen coverage as a function of potential [73,74]. To study this, we used the GC-QM method to calculate the potential-dependent free energy, G, of the (0001) surface at various coverages (ML) and applied potential, U. The free energy as a function of coverage is shown in Fig. 6c for U = 50, 0, and -50 mV_{RHE}. We see that at low potentials, high coverage is favored energetically. This shifts as the potential increases, to favoring low coverage.

The next step was to determine the change in the Tafel barrier as a function of coverage. Fig. 7a, show that the Tafel barrier decreases in going from the minimum coverage of 2/13 to the maximum coverage of 13/13. This is due to near-neighbor repulsion of H, making removal of

H₂ easier. Comparing the four support cases, the graphene case generally has the highest barrier, while the pyrrolic-N case has the lowest. The potentials, U(x), at which the coverage in ML (2/13, 6/13, 9/13, 11/13, 13/13) becomes favorable are plotted in Fig. 7b. We plot the applied potential and the current for each coverage case in Fig. 7c. Based on this Tafel barrier, the current, j(x), was determined using the Eyring equation:

$$j(X) = \frac{n_e q_e C_x}{A} \frac{k_B T}{h} \exp(-\frac{\Delta G_x}{k_B T})$$

where n_e=number of electrons = 2; q_e = electron charge; C_x =surface H concentration = x/13; ΔG_x = predicted free energy activation barrier for the Tafel reaction for coverage x; A = area of cell = $6.4 \times 10^{-16} \text{ cm}^2$.

Fig. 7c shows that pyrrolic-N leads to the most active doped support. The predicted overpotential at which the current reaches - 10 mA/cm² (onset potential) is 24.5 mV_{RHE}. This can be compared to the experimental values of 25.5, 25.4, and 9.6 mV, for the three different N-GPC's (Fig. 4f). It shows the excellent agreement between the average of the three experimental current-potential profiles with the pyrrolic-N case. The onset potential corresponds to a H coverage of 0.49 ML (6.4 H bonded out of 13 sites). Our results show that at these potentials, Ru on top of pyrrolic-N support is the most active for HER. The Ru on top of pyridinic, graphitic, and undoped graphene supports is predicted to be active only at overpotentials greater than 100 mV_{RHE}. In Fig. 7d, the Tafel slope for the Ru on the pyrrolic-N support is predicted to be 27.8 mV/dec in excellent agreement with experimental values of 25.2 mV/dec for Ru/N-GPC (Fig. 5d). This predicts that the superb HER stability of Ru/N-GPC is due to pyrrolic-N in carbon structure as seen in Fig. 5e, f and Fig. S23.

Taking a closer look at why pyrrolic-N support has better

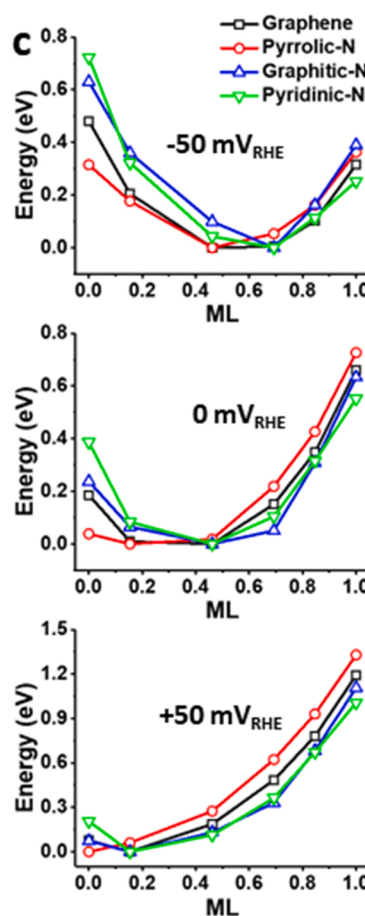
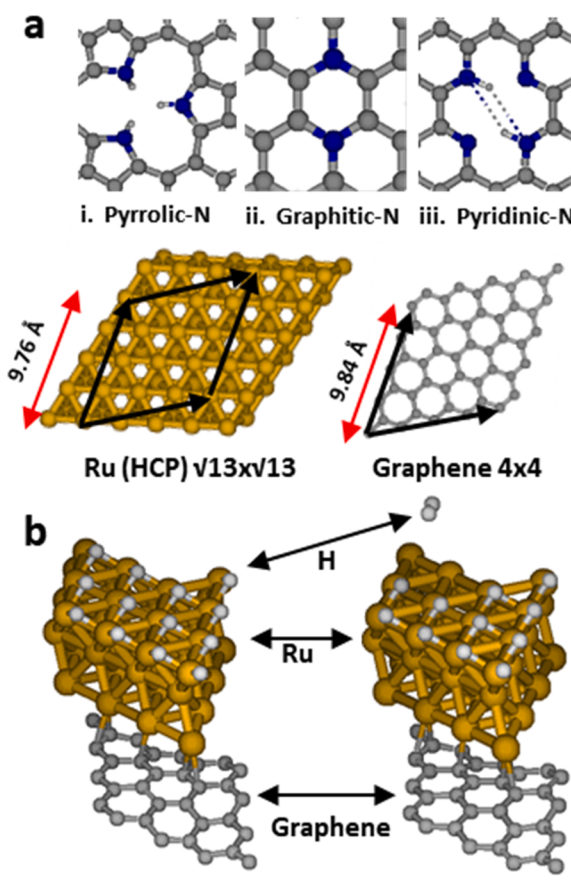


Fig. 6. Hydrogen coverage for supported Ru from DFT calculations. (a) Schematic atomistic pictures of the calculated structures. Grey – C, blue – N, gold – Ru, white – H. Optimized Ru $\sqrt{13}x\sqrt{13}$ has a lattice mismatch of 0.8% versus graphene 4 × 4. (b) Schematic picture of the Tafel reaction for a fully H-saturated Ru surface on a graphene support. (c) The energy as a function of coverage, x/13 ML, for various supports. The three figures are for - 50, 0, and 50 mV_{RHE} at pH 13. We see that more negative potentials favor higher hydrogen coverage.

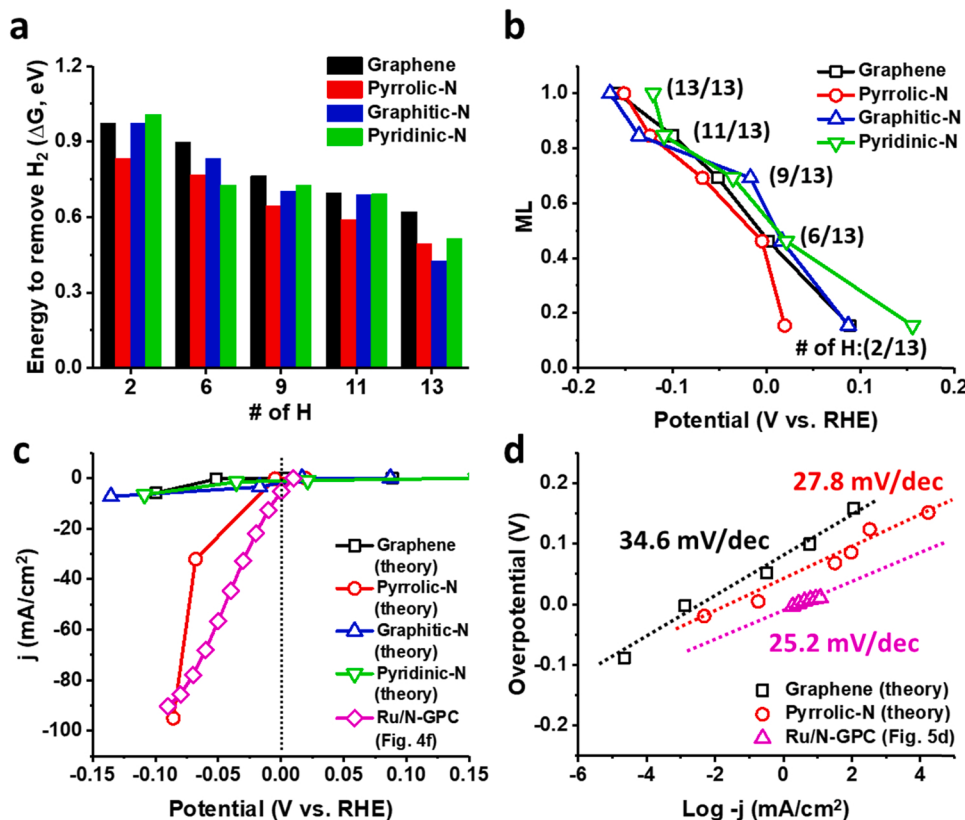


Fig. 7. Predicted HER performance versus support from DFT calculations. (a) Tafel reaction barrier as a function of coverage, $x/13$. The barrier decreases as coverage increases due to near-neighbor repulsion. (b) Plots of H coverage versus Potential, $U(x)$, where $ML = x/13$. (c) Plots of applied potential, $U(x)$, versus current, j (x), calculated from the Eyring equation using the predicted free energy activation barriers, ΔG^\ddagger . The current is dominated by the pyrrolic-N group support. (d) Plots of overpotential (V) vs. $\log -j$ for graphene, pyrrolic-N, and experimental values for N-GPC. The corresponding Tafel slopes are 34.6, 27.8, and 25.2 mV/dec, respectively.

performance than the other three supports, Fig. 7a shows that it is due to the lower binding energy of hydrogen on Ru/pyrrolic-N. This lower binding energy can be explained by examining the strong binding between the support and Ru catalyst. Table S9 displays binding energy and charge of Ru on different N-species supports.

3. Conclusions

In this study, we prepared N-doped extensively graphitized porous carbon (N-GPC) with high pyrrolic-N content by simple reductive pyrolysis of $g\text{-C}_3\text{N}_4$ in the presence of Mg metal, which we used as a catalyst support for Ru NPs to obtain active HER catalysts. Interestingly, the Mg plays a remarkable multiple role not only as a reducing agent for graphitizing the carbon precursor at low temperature (even at 650 °C) but also as a precursor for a new Mg_3N_2 pore-generating agent to offer robust network-structured porous carbon. Open network structure of meso- and macropores for high porosity and large surface area was generated for active interfacial interactions in HER, excellent mass transfer and bubble formation.

We also found that Ru NPs loaded on N-GPC prepared at 950 °C showed an extremely low overpotential of 9.6 mV at a current density of 10 mA/cm² and mass activity of 13.9 mA at 10 A/cm² mg_{metal} (far better than the 39 mV and 73.1 mV for state-of-the-art commercial Pt/C), which led to about 12 times faster TOF for HER than for Pt/C. Furthermore, N-GPC demonstrates superior durability performance while maintaining the low overpotential for 200 h chronopotentiometry and 10,000 CV cycles without any significant degradation. These results indicate near-ideal performance for HER. Grand canonical quantum mechanism (GC-QM) calculation further proves the high concentration of pyrrolic-N groups in the N-GPC leads to superior HER performance of low overpotential and high durability. We attribute the remarkable performance of the Ru/N-GPC to the superior chemical and physical properties of the robust N-GPC support, featuring a high electrical conductivity, the proper amount of N species particularly with high

pyrrolic N content, and the high porosity along with open network-structure.

CRediT authorship contribution statement

Cheol-Hwan Shin: Conceptualization, Methodology, Investigation, Formal analysis, Visualization, Writing – original draft, Writing – review & editing. **Ted H. Yu:** Formal analysis, Methodology, Visualization, Writing – original draft. **Ha-Young Lee:** Formal analysis, Data curation. **Byeong-June Lee:** Formal analysis, Data curation. **Soonho Kwon:** Formal analysis, Data curation. **William A. Goddard III:** Project administration, Funding acquisition, Conceptualization, Supervision, Writing – review & editing. **Jong-Sung Yu:** Project administration, Funding acquisition, Conceptualization, Supervision, Writing – review & editing.

Declaration of Competing Interest

The authors declare the following financial interests/personal relationships which may be considered as potential competing interests: Jong-Sung Yu reports financial support was provided by National Research Foundation of Korea. Jong-Sung Yu reports a relationship with National Research Foundation of Korea that includes: funding grants. The authors declare that they have no other known competing financial interests or personal relationships that could have appeared to influence the work reported in this paper.

Data Availability

Data will be made available on request. Computational data were uploaded to github: https://github.com/tedhyu/Ru_HER.

Acknowledgments

This work was generously supported by the National Research Foundation (2019R1A2C2086770 and 2023K2A9A2A23000259) funded by the Korea Ministry of Science, ICT & Future Planning. Authors would also like to thank the Korean Basic Science Institute (KBSI) at Jeonju and Daejeon for electron microscope analysis. T.H.Y., S.K., and W.A.G. thank ONR (N00014-19-1-2081) for support. The computations presented here were conducted in the Resnick High Performance Center, a facility supported by Resnick Sustainability Institute.

Appendix A. Supporting information

Supplementary data associated with this article can be found in the online version at doi:10.1016/j.apcatb.2023.122829.

References

- [1] T.L. Root, J.T. Price, K.R. Hall, S.H. Schneider, C. Rosenzweig, J.A. Pounds, Fingerprints of global warming on wild animals and plants, *Nature* 421 (2003) 57–60, <https://doi.org/10.1038/nature01333>.
- [2] Y. Kosaka, S.P. Xie, Recent global-warming hiatus tied to equatorial Pacific surface cooling, *Nature* 501 (2013) 403–407, <https://doi.org/10.1038/nature12534>.
- [3] M.E. Dillon, G. Wang, R.B. Huey, Global metabolic impacts of recent climate warming, *Nature* 467 (2010) 704–706, <https://doi.org/10.1038/nature09407>.
- [4] V. Khare, S. Nema, P. Baredar, Solar-wind hybrid renewable energy system: a review, *Renew. Sustain. Energy Rev.* 58 (2016) 23–33, <https://doi.org/10.1016/j.rser.2015.12.223>.
- [5] P.E. Brockway, A. Owen, L.I. Brand-Correa, L. Hardt, Estimation of global final-stage energy-return-on-investment for fossil fuels with comparison to renewable energy sources, *Nat. Energy* 4 (2019) 612–621, <https://doi.org/10.1038/s41560-019-0425-z>.
- [6] Q. Wang, T. Hisatomi, Q. Jia, H. Tokudome, M. Zhong, C. Wang, Z. Pan, T. Takata, M. Nakabayashi, N. Shibata, Y. Li, I.D. Sharp, A. Kudo, T. Yamada, K. Domen, Scalable water splitting on particulate photocatalyst sheets with a solar-to-hydrogen energy conversion efficiency exceeding 1%, *Nat. Mater.* 15 (2016) 611–615, <https://doi.org/10.1038/nmat4589>.
- [7] C.-F. Li, J.-W. Zhao, L.-J. Xie, J.-Q. Wu, Q. Ren, Y. Wang, G.-R. Li, Surface-adsorbed carboxylate ligands on layered double hydroxides/metal–organic frameworks promote the electrocatalytic oxygen evolution reaction, *Angew. Chem. Int. Ed.* 60 (2021) 18129–18137, <https://doi.org/10.1002/anie.202104148>.
- [8] H. Xu, Z.X. Shi, Y.X. Tong, G.R. Li, Porous microrod arrays constructed by carbon-confined NiCo@NiCo₂O₄ core@shell nanoparticles as efficient electrocatalysts for oxygen evolution, *Adv. Mater.* 30 (2018) 1705442, <https://doi.org/10.1002/adma.201705442>.
- [9] J.-X. Feng, H. Xu, Y.-T. Dong, S.-H. Ye, Y.-X. Tong, G.-R. Li, FeOOH/Co/FeOOH hybrid nanobatteries as high-performance electrocatalysts for the oxygen evolution reaction, *Angew. Chem. Int. Ed.* 55 (2016) 3694–3698, <https://doi.org/10.1002/anie.201511447>.
- [10] K. Kunimatsu, T. Senzaki, G. Samjeské, M. Tsushima, M. Osawa, Hydrogen adsorption and hydrogen evolution reaction on a polycrystalline Pt electrode studied by surface-enhanced infrared absorption spectroscopy, *Electrochim. Acta* 52 (2007) 5715–5724, <https://doi.org/10.1016/j.electacta.2006.12.007>.
- [11] E. Skúlason, G.S. Karlberg, J. Rossmeisl, T. Bligaard, J. Greeley, H. Jónsson, J. K. Nørskov, Density functional theory calculations for the hydrogen evolution reaction in an electrochemical double layer on the Pt(111) electrode, *Phys. Chem. Chem. Phys.* 9 (2007) 3241–3250, <https://doi.org/10.1039/b700099e>.
- [12] X. Huang, X. Xu, C. Li, D. Wu, D. Cheng, D. Cao, Vertical CoP nanoarray wrapped by N,P-doped carbon for hydrogen evolution reaction in both acidic and alkaline conditions, *Adv. Energy Mater.* 9 (2019) 1803970, <https://doi.org/10.1002/aenm.201803970>.
- [13] X. Hu, G. Luo, Q. Zhao, D. Wu, T. Yang, J. Wen, R. Wang, C. Xu, N. Hu, Ru Single atoms on N-doped carbon by spatial confinement and ionic substitution strategies for high-performance Li–O₂ batteries, *J. Am. Chem. Soc.* 142 (2020) 16776–16786, <https://doi.org/10.1021/jacs.0c07317>.
- [14] T.V. Vineesh, M.P. Kumar, C. Takahashi, G. Kalita, S. Alwarappan, D. K. Pattanayak, T.N. Narayanan, Bifunctional electrocatalytic activity of boron-doped graphene derived from boron carbide, *Adv. Energy Mater.* 5 (2015) 1500658, <https://doi.org/10.1002/aenm.201500658>.
- [15] Y. Zhou, Y. Leng, W. Zhou, J. Huang, M. Zhao, J. Zhan, C. Feng, Z. Tang, S. Chen, H. Liu, Sulfur and nitrogen self-doped carbon nanosheets derived from peanut root nodules as high-efficiency non-metal electrocatalyst for hydrogen evolution reaction, *Nano Energy* 16 (2015) 357–366, <https://doi.org/10.1016/j.nanoen.2015.07.008>.
- [16] X.-X. Peng, Y.-Q. Lu, L.-L. Zhou, T. Sheng, S.-Y. Shen, H.-G. Liao, L. Huang, J.-T. Li, S.-G. Sun, Graphitized porous carbon materials with high sulfur loading for lithium-sulfur batteries, *Nano Energy* 32 (2017) 503–510, <https://doi.org/10.1016/j.nanoen.2016.12.060>.
- [17] H. Bin Wu, B.Y. Xia, L. Yu, X.Y. Yu, X.W. Lou, Porous molybdenum carbide nano-octahedrons synthesized via confined carburization in metal-organic frameworks for efficient hydrogen production, *Nat. Commun.* 6 (2015) 6512, <https://doi.org/10.1038/ncomms7512>.
- [18] P. Wang, G. Zhang, X.-Y. Wei, R. Liu, J.-J. Gu, F.-F. Cao, Bioselective synthesis of a porous carbon collector for high-performance sodium–metal anodes, *J. Am. Chem. Soc.* 143 (2021) 3280–3283, <https://doi.org/10.1021/jacs.0c12098>.
- [19] X. Liu, Y. Hao, J. Shu, H.M.K. Sari, L. Lin, H. Kou, J. Li, W. Liu, B. Yan, D. Li, J. Zhang, X. Li, Nitrogen/sulfur dual-doping of reduced graphene oxide harvesting hollow ZnSnS₃ nano-microcubes with superior sodium storage, *Nano Energy* 57 (2019) 414–423, <https://doi.org/10.1016/j.nanoen.2018.12.024>.
- [20] J. Deng, P. Ren, D. Deng, L. Yu, F. Yang, X. Bao, Highly active and durable non-precious-metal catalysts encapsulated in carbon nanotubes for hydrogen evolution reaction, *Energy Environ. Sci.* 7 (2014) 1919–1923, <https://doi.org/10.1039/c4ee00370e>.
- [21] S. Du, Z. Ren, J. Zhang, J. Wu, W. Xi, J. Zhu, H. Fu, Co₃O₄ nanocrystal ink printed on carbon fiber paper as a large-area electrode for electrochemical water splitting, *Chem. Commun.* 51 (2015) 8066–8069, <https://doi.org/10.1039/c5cc01080b>.
- [22] T. Xia, W. Zhang, Z. Wang, Y. Zhang, X. Song, J. Murowick, V. Battaglia, G. Liu, X. Chen, Amorphous carbon-coated TiO₂ nanocrystals for improved lithium-ion battery and photocatalytic performance, *Nano Energy* 6 (2014) 109–118, <https://doi.org/10.1016/j.nanoen.2014.03.012>.
- [23] W. Luo, Y. Wang, C. Cheng, Ru-based electrocatalysts for hydrogen evolution reaction: Recent research advances and perspectives, *Mater. Today Phys.* (2020), 100274, <https://doi.org/10.1016/j.mtphys.2020.100274>.
- [24] S. Ye, F. Luo, T. Xu, P. Zhang, H. Shi, S. Qin, J. Wu, C. He, X. Ouyang, Q. Zhang, Boosting the alkaline hydrogen evolution of Ru nanoclusters anchored on B/N-doped graphene by accelerating water dissociation, *Nano Energy* 68 (2020), 104301, <https://doi.org/10.1016/j.nanoen.2019.104301>.
- [25] F. Li, G.F. Han, H.J. Noh, I. Ahmad, I.Y. Jeon, J.B. Baek, Mechanochemically assisted synthesis of a Ru catalyst for hydrogen evolution with performance superior to Pt in both acidic and alkaline Media, *Adv. Mater.* 30 (2018) 1803676, <https://doi.org/10.1002/adma.201803676>.
- [26] B. Lu, L. Guo, F. Wu, Y. Peng, J.E. Lu, T.J. Smart, N. Wang, Y.Z. Finfrock, D. Morris, P. Zhang, N. Li, P. Gao, Y. Ping, S. Chen, Ruthenium atomically dispersed in carbon outperforms platinum toward hydrogen evolution in alkaline media, *Nat. Commun.* 10 (2019) 631, <https://doi.org/10.1038/s41467-019-08419-3>.
- [27] H.-Y. Lee, T.H. Yu, C.-H. Shin, A. Fortunelli, S.G. Ji, Y. Kim, T.-H. Kang, B.-J. Lee, B. V. Merinov, W.A. Goddard, C.H. Choi, J.-S. Yu, Low temperature synthesis of new highly graphitized N-doped carbon for Pt fuel cell supports satisfying DOE 2025 durability standards for both catalyst and support, *Appl. Catal. B Environ.* 323 (2023), 122179, <https://doi.org/10.1016/j.apcatb.2022.122179>.
- [28] Z. Qiao, S. Hwang, X. Li, C. Wang, W. Samarakoon, S. Karakalos, D. Li, M. Chen, Y. He, M. Wang, 3D porous graphitic nanocarbon for enhancing the performance and durability of Pt catalysts: a balance between graphitization and hierarchical porosity, *Energy Environ. Sci.* 12 (2019) 2830–2841, <https://doi.org/10.1039/c9ee01899a>.
- [29] H. Zhang, H. Ming, W. Zhang, G. Cao, Y. Yang, Coupled carbonization strategy toward advanced hard carbon for high-energy sodium-ion battery, *ACS Appl. Mater. Interfaces* 9 (2017) 23766–23774, <https://doi.org/10.1021/acsmi.7b05687>.
- [30] Z. Yan, M. Cai, P.K. Shen, Low temperature formation of porous graphitized carbon for electrocatalysis, *J. Mater. Chem.* 22 (2012) 2133–2139, <https://doi.org/10.1039/CJHM14765J>.
- [31] S.B. Yoon, G.S. Chai, S.K. Kang, J.-S. Yu, K.P. Gierszal, M. Jaroniec, Graphitized pitch-based carbons with ordered nanopores synthesized by using colloidal crystals as templates, *J. Am. Chem. Soc.* 127 (2005) 4188–4189, <https://doi.org/10.1021/acsmi.7b05687>, <https://doi.org/10.1021/ja0423466>.
- [32] B. Fang, J.H. Kim, M.-S. Kim, J.-S. Yu, Hierarchical nanostructured carbons with meso–macroporosity: design, characterization, and applications, *Acc. Chem. Res.* 46 (2013) 1397–1406, <https://doi.org/10.1021/ar300253f>.
- [33] Y. Ding, C. Yu, J. Chang, C. Yao, J. Yu, W. Guo, J. Qiu, Effective fixation of carbon in g-C₃N₄ enabled by Mg-Induced selective reconstruction, *Small* 16 (2020) 1907164, <https://doi.org/10.1002/smll.201907164>.
- [34] A. Kamiyama, K. Kubota, D. Igashira, Y. Youn, Y. Tateyama, H. Ando, K. Gotoh, S. Komaba, MgO-template synthesis of extremely high capacity hard carbon for Na-ion battery, *Angew. Chem. Int. Ed.* 60 (2021) 5114–5120, <https://doi.org/10.1002/ange.202013951>.
- [35] X. Lu, H. Xu, P. Yang, L. Xiao, Y. Li, J. Ma, R. Li, L. Liu, A. Liu, V. Kondratiev, Zinc-assisted MgO template synthesis of porous carbon-supported Fe-N_x sites for efficient oxygen reduction reaction catalysis in Zn-air batteries, *Appl. Catal. B Environ.* 313 (2022), 121454, <https://doi.org/10.1016/j.apcatb.2022.121454>.
- [36] E. Negro, K. Vezzù, F. Bertasi, P. Schiavuta, L. Toniolo, S. Polizzi, V. Di Noto, Interplay between nitrogen concentration, structure, morphology, and electrochemical performance of PdCoNi “core–shell” carbon nitride electrocatalysts for the oxygen reduction reaction, *ChemElectroChem* 1 (2014) 1359–1369, <https://doi.org/10.1002/celec.201402041>.
- [37] C.-H. Shin, H.-Y. Lee, C. Gyan-Barimah, J.-H. Yu, J.-S. Yu, Magnesium: properties and rich chemistry for new material synthesis and energy applications, *Chem. Soc. Rev.* 52 (2023) 2145–2192, <https://doi.org/10.1039/D2CS00810F>.
- [38] A. Sinhamahapatra, J.P. Jeon, J.-S. Yu, A new approach to prepare highly active and stable black titania for visible light-assisted hydrogen production, *Energy Environ. Sci.* 8 (2015) 3539–3544, <https://doi.org/10.1039/c5ee02443a>.
- [39] A. Sinhamahapatra, J.P. Jeon, J. Kang, B. Han, J.-S. Yu, Oxygen-deficient zirconia (ZrO_{2-x}): a new material for solar light absorption, *Sci. Rep.* 6 (2016) 27218, <https://doi.org/10.1038/srep27218>.
- [40] G. Park, C.-H. Shin, J. Kang, K.-S. Lee, C. Zhang, B. Lim, C. Kim, J.-S. Yu, Controllable synthesis of single-layer graphene over cobalt nanoparticles and

- insight into active sites for efficient oxygen evolution, *J. Mater. Chem. A* 9 (2021) 12060–12073, <https://doi.org/10.1039/d1ta02677a>.
- [41] J. Liu, T. Zhang, Z. Wang, G. Dawson, W. Chen, Simple pyrolysis of urea into graphitic carbon nitride with recyclable adsorption and photocatalytic activity, *J. Mater. Chem. B* 21 (2011) 14398–14401, <https://doi.org/10.1039/c1jm12620b>.
- [42] A.C. Ferrari, J.C. Meyer, V. Scardaci, C. Casiraghi, M. Lazzeri, F. Mauri, S. Piscanec, D. Jiang, K.S. Novoselov, S. Roth, Raman spectrum of graphene and graphene layers, *Phys. Rev. Lett.* 97 (2006), 187401, <https://doi.org/10.1103/physrevlett.97.187401>.
- [43] Y.Y. Wang, Z.H. Ni, Z.X. Shen, H.M. Wang, Y.H. Wu, Interference enhancement of Raman signal of graphene, *Appl. Phys. Lett.* 92 (2008), 043121, <https://doi.org/10.1063/1.283745>.
- [44] W. Chen, J. Pei, C.T. He, J. Wan, H. Ren, Y. Zhu, Y. Wang, J. Dong, S. Tian, W. C. Cheong, S. Lu, L. Zheng, X. Zheng, W. Yan, Z. Zhuang, C. Chen, Q. Peng, D. Wang, Y. Li, Rational design of single molybdenum atoms anchored on N-doped carbon for effective hydrogen evolution reaction, *Angew. Chem. Int. Ed.* 56 (2017) 16086–16090, <https://doi.org/10.1002/anie.201710599>.
- [45] S.K. Singh, K. Takeyasu, J. Nakamura, Active sites and mechanism of oxygen reduction reaction electrocatalysis on nitrogen-doped carbon materials, *Adv. Mater.* 31 (2019) 1804297, <https://doi.org/10.1002/adma.201804297>.
- [46] M.Y. Song, D.S. Yang, K.P. Singh, J. Yuan, J.-S. Yu, Nitrogen-doped hollow carbon spheres with highly graphitized mesoporous shell: Role of Fe for oxygen evolution reaction, *Appl. Catal. B Environ.* 191 (2016) 202–208, <https://doi.org/10.1016/j.apcatb.2016.03.031>.
- [47] A. Walcarius, Mesoporous materials and electrochemistry, *Chem. Soc. Rev.* 42 (2013) 4098–4140, <https://doi.org/10.1039/c2cs35322a>.
- [48] D.S. Yang, D. Bhattacharjya, S. Inamdar, J. Park, J.-S. Yu, Phosphorus-doped ordered mesoporous carbons with different lengths as efficient metal-free electrocatalysts for oxygen reduction reaction in alkaline media, *J. Am. Chem. Soc.* 134 (2012) 16127–16130, <https://doi.org/10.1021/ja306376s>.
- [49] Y. Sun, Z. Xue, Q. Liu, Y. Jia, Y. Li, K. Liu, Y. Lin, M. Liu, G. Li, C.-Y. Su, Modulating electronic structure of metal-organic frameworks by introducing atomically dispersed Ru for efficient hydrogen evolution, *Nat. Commun.* 12 (2021) 1369, <https://doi.org/10.1038/s41467-021-21595-5>.
- [50] O. Tanaike, H. Hatori, Y. Yamada, S. Shiraishi, A. Oya, Preparation and pore control of highly mesoporous carbon from defluorinated PTFE, *Carbon N.* 41 (2003) 1759–1764, [https://doi.org/10.1016/S0008-6223\(03\)00146-5](https://doi.org/10.1016/S0008-6223(03)00146-5).
- [51] D.C. Marcano, D.V. Kosynkin, J.M. Berlin, A. Sinitskii, Z. Sun, A. Slesarev, L. B. Alemany, W. Lu, J.M. Tour, Improved synthesis of graphene oxide, *ACS Nano* 4 (2010) 4806–4814, <https://doi.org/10.1021/nn1006368>.
- [52] H.Q. Fu, M. Zhou, P.F. Liu, P. Liu, H. Yin, K.Z. Sun, H.G. Yang, M. Al-Mamun, P. Hu, H.-F. Wang, Hydrogen spillover-bridged Volmer/Tafel processes enabling ampere-level current density alkaline hydrogen evolution reaction under low overpotential, *J. Am. Chem. Soc.* 144 (2022) 6028–6039, <https://doi.org/10.1021/jacs.2c01094.s001>.
- [53] H. Wang, X. Li, Q. Ruan, J. Tang, Ru and RuO_x decorated carbon nitride for efficient ammonia photosynthesis, *Nanoscale* 12 (2020) 12329–12335, <https://doi.org/10.1039/DONR02527E>.
- [54] J. Kärger, R. Valiullin, Mass transfer in mesoporous materials: the benefit of microscopic diffusion measurement, *Chem. Soc. Rev.* 42 (2013) 4172–4197, <https://doi.org/10.1039/c3cs35326e>.
- [55] Z. Chen, Y. Qin, D. Weng, Q. Xiao, Y. Peng, X. Wang, H. Li, F. Wei, Y. Lu, Design and synthesis of hierarchical nanowire composites for electrochemical energy storage, *Adv. Funct. Mater.* 19 (2009) 3420–3426, <https://doi.org/10.1002/adfm.200900971>.
- [56] J. Mahmood, F. Li, S.M. Jung, M.S. Okuyay, I. Ahmad, S.J. Kim, N. Park, H.Y. Jeong, J.B. Baek, An efficient and pH-universal ruthenium-based catalyst for the hydrogen evolution reaction, *Nat. Nanotechnol.* 12 (2017) 441–446, <https://doi.org/10.1038/nano.2016.304>.
- [57] Q. Chang, J. Ma, Y. Zhu, Z. Li, D. Xu, X. Duan, W. Peng, Y. Li, G. Zhang, F. Zhang, X. Fan, Controllable synthesis of ruthenium phosphides (RuP and RuP₂) for pH-universal hydrogen evolution reaction, *ACS Sustain. Chem. Eng.* 6 (2018) 6388–6394, <https://doi.org/10.1021/acssuschemeng.8b00187>.
- [58] P. Li, X. Duan, S. Wang, L. Zheng, Y. Li, H. Duan, Y. Kuang, X. Sun, Amorphous ruthenium-sulfide with isolated catalytic sites for Pt-like electrocatalytic hydrogen production over whole pH range, *Small* 15 (2019) 1904043, <https://doi.org/10.1002/smll.201904043>.
- [59] J. Xu, T. Liu, J. Li, B. Li, Y. Liu, B. Zhang, D. Xiong, I. Amorim, W. Li, L. Liu, Boosting the hydrogen evolution performance of ruthenium clusters through synergistic coupling with cobalt phosphide, *Energy Environ. Sci.* 11 (2018) 1819–1827, <https://doi.org/10.1039/c7ee03603e>.
- [60] M. Li, H. Wang, W. Zhu, W. Li, C. Wang, X. Lu, RuNi nanoparticles embedded in N-doped carbon nanofibers as a robust bifunctional catalyst for efficient overall water splitting, *Adv. Sci. Sci.* 7 (2020) 1901833, <https://doi.org/10.1002/advs.201901833>.
- [61] J. Su, Y. Yang, G. Xia, J. Chen, P. Jiang, Q. Chen, Ruthenium-cobalt nanoalloys encapsulated in nitrogen-doped graphene as active electrocatalysts for producing hydrogen in alkaline media, *Nat. Commun.* 8 (2017) 14969, <https://doi.org/10.1038/ncomms14969>.
- [62] J. Mao, C.T. He, J. Pei, W. Chen, D. He, Y. He, Z. Zhuang, C. Chen, Q. Peng, D. Wang, Y. Li, Accelerating water dissociation kinetics by isolating cobalt atoms into ruthenium lattice, *Nat. Commun.* 9 (2018) 4958, <https://doi.org/10.1038/s41467-018-07288-6>.
- [63] J.Q. Chi, W.K. Gao, J.H. Lin, B. Dong, K.L. Yan, J.F. Qin, B. Liu, Y.M. Chai, C.G. Liu, Hydrogen evolution activity of ruthenium phosphides encapsulated in nitrogen- and phosphorous-codoped hollow carbon nanospheres, *ChemSusChem* 11 (2018) 743–752, <https://doi.org/10.1002/cssc.201702010>.
- [64] D. Wang, Q. Li, C. Han, Z. Xing, X. Yang, Single-atom ruthenium based catalyst for enhanced hydrogen evolution, *Appl. Catal. B Environ.* 249 (2019) 91–97, <https://doi.org/10.1016/j.apcatb.2019.02.059>.
- [65] C.H. Chen, D. Wu, Z. Li, R. Zhang, C.G. Kuai, X.R. Zhao, C.K. Dong, S.Z. Qiao, H. Liu, X.W. Du, Ruthenium-based single-atom alloy with high electrocatalytic activity for hydrogen evolution, *Adv. Energy Mater.* 9 (2019) 1803913, <https://doi.org/10.1002/aenm.201803913>.
- [66] J. Creus, J. De Tovar, N. Romero, J. García-Antón, K. Philippot, R. Bofill, X. Sala, Ruthenium nanoparticles for catalytic water splitting, *ChemSusChem* 12 (2019) 2493–2514, <https://doi.org/10.1002/cssc.201900393>.
- [67] J.P. Perdew, K. Burke, M. Ernzerhof, Generalized gradient approximation made simple, *Phys. Rev. Lett.* 77 (1996) 3865–3868, <https://doi.org/10.1103/PhysRevLett.77.3865>.
- [68] S. Grimme, J. Antony, S. Ehrlich, H. Krieg, A consistent and accurate ab initio parametrization of density functional dispersion correction (DFT-D) for the 94 elements H–Pu, *J. Chem. Phys.* 132 (2010), 154104, <https://doi.org/10.1063/1.3382344>.
- [69] X.-Y. Zhang, J.-Y. Xie, Y. Ma, B. Dong, C.-G. Liu, Y.-M. Chai, An overview of the active sites in transition metal electrocatalysts and their practical activity for hydrogen evolution reaction, *Chem. Eng. J.* 430 (2022), 132312, <https://doi.org/10.1016/j.cej.2021.132312>.
- [70] Y. Huang, R.J. Nielsen, W.A. Goddard III, Reaction mechanism for the hydrogen evolution reaction on the basal plane sulfur vacancy site of MoS₂ using grand canonical potential kinetics, *J. Am. Chem. Soc.* 140 (2018) 16773–16782, <https://doi.org/10.1021/jacs.8b10016.s001>.
- [71] M.D. Hossain, Y. Huang, H.Y. Ted, W.A. Goddard III, Z. Luo, Reaction mechanism and kinetics for CO₂ reduction on nickel single atom catalysts from quantum mechanics, *Nat. Commun.* 11 (2020) 1064, <https://doi.org/10.1038/s41467-020-16119-6>.
- [72] N.M. Marković, B.N. Grgur, P.N. Ross, Temperature-dependent hydrogen electrochemistry on platinum low-index single-crystal surfaces in acid solutions, *J. Phys. Chem. B* 101 (1997) 5405–5413, <https://doi.org/10.1021/jp970930d>.
- [73] Y.-H. Fang, Z.-P. Liu, Tafel kinetics of electrocatalytic reactions: from experiment to first-principles, *ACS Catal.* 4 (2014) 4364–4376, <https://doi.org/10.1021/cs501312v>.
- [74] T. Shinagawa, A.T. Garcia-Esparza, K. Takanabe, Insight on Tafel slopes from a microkinetic analysis of aqueous electrocatalysis for energy conversion, *Sci. Rep.* 5 (2015) 13801, <https://doi.org/10.1038/srep13801>.